Understanding Backgrounds: Suppression of Non-Prompt Leptons for the ATLAS Detector at the Large Hadron Collider

Senior Thesis

Iria Wang

May 2022

Advised by Dr. Gabriella Sciolla

A thesis presented for the degree of
Bachelors of Science in Physics

Martin A. Fisher School of Physics
Brandeis University
Waltham, MA

May 11, 2025

Presented to
The Faculty of the School of Arts and Sciences
Brandeis University

Undergraduate Program in Physics
Gabriella Sciolla, Advisor

In partial fulfillment of the requirements for the degree of Bachelor of Science

Committee Member: ______________________________

Gabriella Sciolla, Ph.D.
Professor of Physics

Committee Member: ______________________________

Aram Apyan, Ph.D.
Assistant Professor of Physics

Abstract

The proton-proton collisions occurring inside the ATLAS experiment at the Large Hadron Collider in CERN result in an ever-growing dataset with increasing statistical precision, thus requiring a precise understanding of background sources. Four-lepton events, which have final states of two same-flavor, opposite-charge electron or muon pairs, present ideal candidates for high-precision studies of the Standard Model of Particle Physics due to interesting contributions from processes within and beyond the Standard Model. However, non-prompt leptons, produced by event mis-reconstructions or secondary decays of hadrons, contaminate the sample. These backgrounds include rare detector effects and therefore are preferentially studied using data-driven methods. A sample of real dilepton collision data, in which additional leptons likely appear as non-prompt, is studied through comparisons with Monte Carlo simulated data. Samples of Z boson and top quark pair decays are selected. These samples are used to test background suppression requirements, estimate residual non-prompt sources, and reduce background measurement uncertainties.

1 Theory

1.1 Background

1.1.1 Quantum Field Theory

Areas of physics are defined by energy and speed. The defining constants are the speed of light in vacuum, c, and Plank's constant, $h = 2\pi\hbar$. For speeds much less than c and energies much greater than $\hbar$, Classical Mechanics applies. For speeds close to c, Special Relativity applies. For energies close to $\hbar$, Quantum Mechanics applies. In the intersection of Special Relativity and Quantum Mechanics, where speeds are close to c and energies are close to $\hbar$, Quantum Field Theory (QFT) applies. As a mathematically consistent combination of Special Relativity and Quantum Mechanics, QFT is a general framework used to describe subatomic particles and their interactions [10]. The research presented falls in this category.

Special Relativity, first proposed by Albert Einstein in 1905, describes the relationship between space and time and is based on two postulates:

1. Physical laws are invariant in all inertial reference frames, that is, frames of reference with no acceleration.
2. Speed of light in vacuum, $c = 299,792,458$ meters per second, is constant in all frames of reference.

Space-time coordinate transformations, or Lorentz transformations, for a primed inertial frame moving with constant velocity v along the x axis relative to another inertial reference frame, are formulated as

$$ct' = \gamma(ct - \beta x),\ x' = \gamma(x - \beta ct),\ y' = y,\ z' = z \tag{1}$$

$$\text{where } \beta = \frac{v}{c},\ \gamma = \frac{1}{\sqrt{1-\beta^2}}$$

Mathematically, physical observables are represented as energy-momentum contravariant four-vectors $p^\mu = (E/c, \overrightarrow{p})$ and covariant vectors $p_\mu = (E/c, -\overrightarrow{p})$, with energy $E = \gamma mc^2$ and momentum $\overrightarrow{p} = \gamma m \overrightarrow{v}$ [10].

The product of the four-vectors yields the famous result:

$$p^\mu p_\mu = E^2/c^2 - \overrightarrow{p}^2 \implies E^2 = \overrightarrow{p}^2 c^2 + m^2 c^4. \tag{2}$$

Quantum Mechanics, developed in the 1900s, describes physics at small scales as quantized particles or continuous waves. Systems have a spectrum of ground and excited energy states. Information about a given energy state of a system is encoded by the complex-valued wave function $\Psi(\overrightarrow{x}, t)$. Wave functions must satisfy the Schrodinger equation,

$$i\hbar\frac{\partial}{\partial t}\Psi(x,t) = \hat{H}\Psi(x,t), \tag{3}$$

where the Hamiltonian operator is,

$$\hat{H} = \frac{\hbar^2}{2m}\nabla^2 + V(\overrightarrow{x}, t). \tag{4}$$

Note that $\hbar = h/2\pi = 1.054571817 \times 10^{-34}$ J·s and $V(\overrightarrow{x}, t)$ is the potential energy of the system [11].

QFT combines these concepts, and treats particles as discrete quanta of underlying quantum fields. It is often convenient to set $c = \hbar = 1$. QFT is formulated with the Lagrangian, which consists of energy and interactions terms that describe interactions between particles. Interactions are graphically represented using Feynman diagrams, where each line is a particle and each vertex is an interaction.

1.1.2 The Standard Model

The Standard Model (SM) of Particle Physics is an extensively tested and validated QFT that describes fundamental particles and the three fundamental forces with which they interact: the strong, weak, and electromagnetic forces. Particles are identified as *fermions*, which make up visible matter, *gauge bosons*, or force carriers, and the Higgs *scalar boson*, which couples to mass. Fermions are further categorized into quarks and leptons based on the forces with which they interact. Each boson mediates one of the fundamental forces or, in the case of the Higgs, the mass-attributing Higgs field[10]. These constituents are summarized in Figure 1 and Table 1.

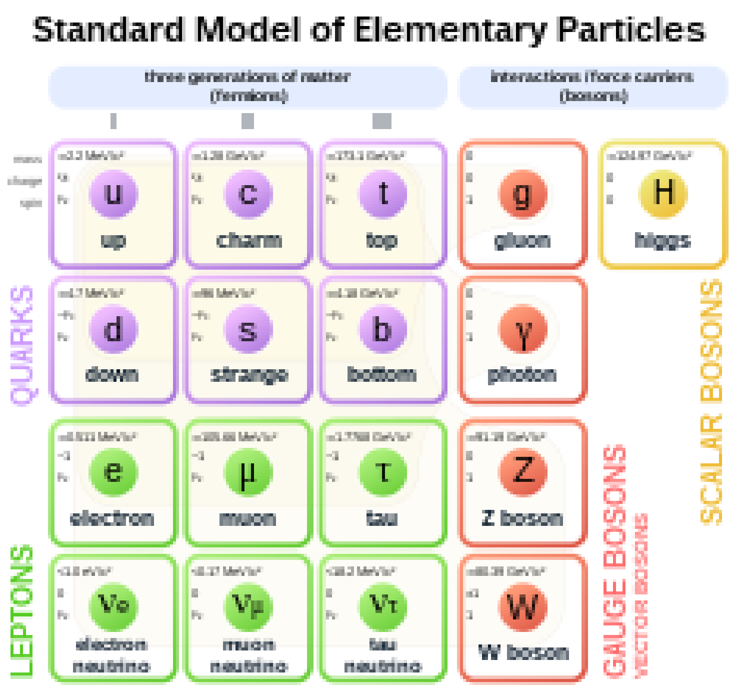

Figure 1: Table of elements in the Standard Model of Particle Physics, organized by generations and other properties. (*Wikipedia*)

Particles within fermion categories are divided into three generations each, with higher generations having increasingly greater mass. Higher generations are also increasingly unstable. Ordinary matter only consists of the first generation, namely the electron as well as up and down quarks in protons (uud) and neutrons (udd).

The three interactions – strong, electromagnetic, and weak – are based on local gauge symmetries and described using laws of conservation. Quantum Chromodynamics (QCD) is the theory of strong interactions and has local SU(3) gauge symmetry of color charge. QCD implies the existence of eight gluons, and that quarks may come in three colors. These particles only exist in the real world as

Category		Name	Symbol	Spin	Charge	Mass	Interaction Force/Field
Bosons	Scalar	Higgs	H	0	0	125.25 GeV	Higgs field
	Gauge	Gluon	g	1	0	0	strong
		Photon	γ	1	0	0	electromagnetic
		Z Boson	Z	1	0	91.19 GeV	weak
		W Boson	$W^{\pm}$	1	±1	80.38 GeV	
Fermions	Quarks	Up	u	1/2	$\pm2/3$	2.16 MeV	strong, electromagnetic, weak
		Down	d	1/2	$\mp1/3$	4.67 MeV	
		Charm	c	1/2	$\pm2/3$	1.27 GeV	
		Strange	s	1/2	$\mp1/3$	93 MeV	
		Top	t	1/2	$\pm2/3$	173 GeV	
		Bottom	b	1/2	$\mp1/3$	4.18 GeV	
	Leptons	Electron	e	1/2	∓1	0.511 MeV	electromagnetic, weak
		Muon	μ	1/2	∓1	105.66 MeV	
		Tau	τ	1/2	∓1	1776.86 MeV	
		e-neutrino	ν_e	1/2	0	< 1.1 eV	weak
		μ-neutrino	ν_μ	1/2	0	< 0.19 MeV	
		τ-neutrino	ν_τ	1/2	0	< 18.2 MeV	

Table 1: A Summary of Standard Model Particles. The properties given are category, particle name, symbol, spin, charge, mass, and the field or force that the specified boson mediates or specified fermion interacts with. Charge is in units of elementary charge, and the mass is from the 2020 summary tables provided by the Particle Data Group. Particle-antiparticle pairs are listed together [8].

singlets, or colorless combinations of quarks and gluons, and are called hadrons and baryons. This result is called color confinement. Quantum Electrodynamics (QED) is the theory of electromagnetic interactions. The electroweak theory unifies electromagnetic and weak interactions with SU(2)$_L$ $\times$ U(1) local gauge symmetry. This symmetry is spontaneously broken, which leads to a U(1) symmetry corresponding to the photon and massive gauge bosons Z and $W^{\pm}$. There also must be a scalar Higgs boson, which couples to mass [10].

The full Lagrangian for the SM is a multi-page equation, but can be summarized as such:

$$\mathcal{L}_{SM} = -\frac{1}{4}F_{\mu\nu}F^{\mu\nu} + i\bar{\psi}\gamma^{\mu}D_{\mu}\psi + \bar{\psi}_i y_{ij}\psi_j\phi + (\bar{\psi}_i y_{ij}\psi_j\phi)^{\dagger} + |D_{\mu}\phi|^2 - V(\psi).$$

The first term encapsulates the dynamics of and interactions between bosons, described by the scalar product of the field strenth tensor, $F_{\mu\nu}$. Fermionic interactions mediated by gauge bosons are described by the second term, where ψ is the fermion field and $\gamma^{\mu}D_{\mu}$ is the so-called covariant derivative. The third and fourth terms are Higgs-fermion couplings. The Higgs field ϕ couples to fermions and antifermions with coupling parameters from the Yukawa matrix, y_{ij}, generating mass for fermionic particles. The fifth term describes the interaction between gauge bosons and the Higgs field, and explains the non-zero masses of W and Z bosons. The sixth term represents the Higgs potential and its self-couplings [13].

Interactions are quantified by a host of SM-specific constants for different types of forces and interactions. For individual interactions and decay modes, these constants are used to compute cross sections σ and branching fractions. Interactions occur with certain probabilities, measured by the cross section, which has units of length squared (1 barn = 1 b = 10^{-24} cm^2) and depends on the corresponding interaction terms of the Lagrangian. The branching ratio describes the probability that a particle may decay through a specific mode, and is calculated using the decay width Γ, in units of inverse seconds.

1.1.3 Beyond the Standard Model

The previously theorized Higgs boson was the final puzzle piece of the SM, and its discovery in 2012 at the Large Hadron Collider (LHC) in Geneva, Switzerland completed the theory. While the completed SM very effectively and accurately describes known particles and their interactions, there are several questions that remain to be solved. The following are a few arguments that suggest the existence of new physics Beyond the Standard Model (BSM).

- Measurements of rotational speeds of stars in galaxies suggest the existence of non-visible mass, called dark matter. It is estimated that dark matter comprises 24 percent of energy density in the universe, while baryonic visible matter makes up just 5 percent. Dark matter is missing from the current understanding of particle physics. One theory is that dark matter is made up of weakly interacting massive particles (WIMPs), but the modern SM has no particle with such properties.
- While matter and antimatter particles are expected to have been produced in equal quantities during the Big Bang, the universe today consists primarily of matter, and the cause of this is yet to be understood.
- The origin of electroweak symmetry breaking, which gives rise to the massive W and Z bosons as well as the Higgs, is not explained by the SM.
- The fourth and final fundamental force of the universe, gravity, is excluded from the SM.
- The properties of neutrino masses and oscillations are not fully understood.
- Researchers also question aesthetic issues within the SM, such as the large number of parameters, the existence of generations, and why the gauge and mass structures are the way they are.

These topics provide motivation in the search for new physics beyond the SM. One very popular extension of the SM is the theory of Supersymmetry (SUSY), which is based on a possible space-time symmetry that couples particles that differ by half a unit of spin. This theory is mathematically beautiful and would resolve several issues within the SM.

1.2 Four-Lepton Processes

Four-lepton decay channels, which result in a final state of two same-flavor, opposite-charge lepton pairs, present an ideal probe of the Standard Model. Several interesting SM processes contribute to the production of four leptons through intermediary massive gauge bosons, which provide insights into an important aspect of electroweak symmetry breaking. These processes include single Z boson production, Higgs boson production, and on-shell ZZ production. These rare processes are also sensitive to the effects of processes beyond the SM. The signature generally allows for a clean separation from backgrounds.

1.2.1 Standard Model Contributions

Shown in Figure 2, there are four leading order dominant modes of SM four-lepton production resulting from high energy hadronic interactions. These processes were observed as events in ATLAS experiment at the Large Hadron Collider.

These multi-boson processes, that is, processes mediated by two or more massive gauge bosons, are crucial for precision tests of the SM in collider experiments due to their couplings to electroweak symmetry breaking, allowing direct testing of non-Abelian gauge theories [13] [9]. The leptonic decay channel also has particularly clean separation between processes of interest and otherwise overwhelming backgrounds.

To identify these processes, events are selected from reconstructed ATLAS collision data using a carefully developed series of selection criteria. The same criteria is applied to data produced by Monte Carlo simulation of the ATLAS detector for comparison, with the key difference that the process a datum originates from is known from the simulation. The four-lepton invariant mass $m_{4\ell}$ distribution for selections of collision and simulation data are shown in Figure 3.

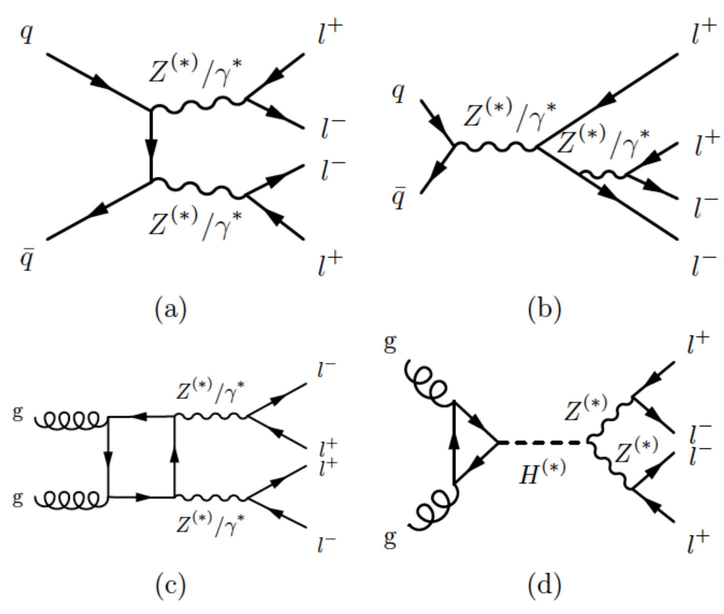

Figure 2: Representative leading order Feynman diagrams for the dominant modes of Standard Model four-lepton production at high energy hadron colliders. The superscript * denotes that the particle is off the mass shell, while (*) indicates the particle can be on-shell or off-shell [13].

The dominant mode is the t-channel $q\bar{q} \to 4\ell$ production in Figure 2a, occurring via two intermediate Z bosons. The Z bosons then decay as $Z \to \ell^+\ell^-$, with a branching fraction of approximately 10 percent in the SM [13]. These events appear in red in Figure 3 for masses above approximately 200 GeV.

Figure 2b shows $q\bar{q} \to Z \to 4\ell$ where a Z boson decays to a lepton pair and the final state radiation from of of the leptons produces the second lepton pair [6]. This process accounts for the peak in Figure 3 around the mass of a Z boson, i.e. about 91 GeV.

The gluon-induced production of bosons through an intermediary quark loop in Figure 2c and in orange in Figure 3 contributes as next-to-next-to leading order relative to the quark-induced process in strong coupling [6].

Near the Higgs mass there is a Higgs mediated s-channel production of $H \to ZZ \to 4\ell$ through the dominant gluon fusion mode in Figure 2d [6]. This was one of the decay modes used in the discovery of the Higgs boson at the Large Hadron Collider in 2012, and can be seen as the blue peak around the Higgs boson mass at 125 GeV in Figure 3.

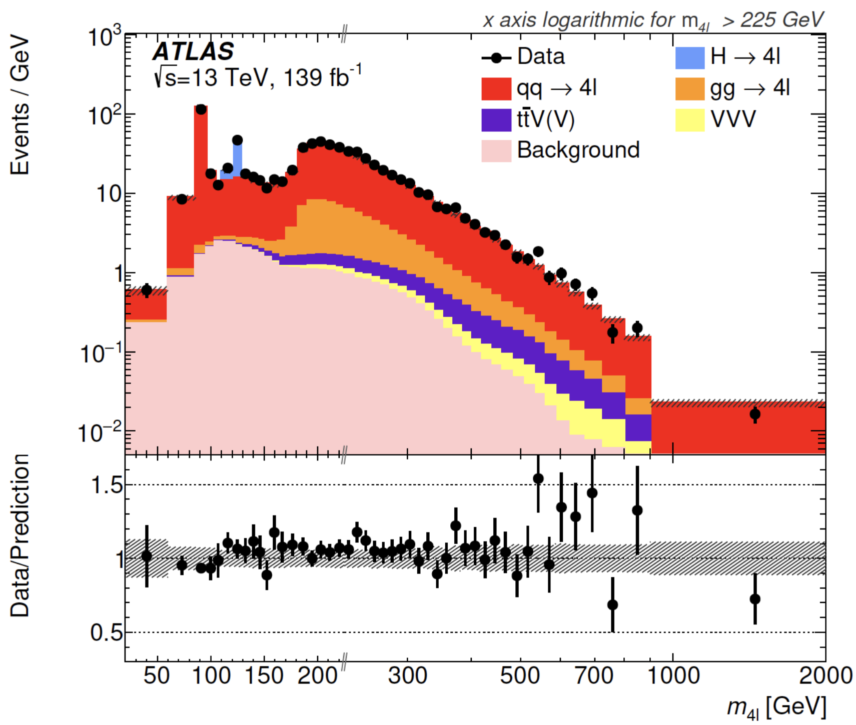

Figure 3: Histogram and ratio plot of various four-lepton contributions is the ATLAS Experiment at the Large Hadron Collider at CERN. Black points are data, and the colors are stacked histograms of Monte Carlo simulated predictions [6].

While the four dominant channels from Figure 2 represent the primary physics processes of interest, prompt backgrounds resulting from top quark pair ($t\bar{t}$) decays and so-called non-prompt lepton backgrounds remain. The $t\bar{t}$ events probe another collision environment and are shown in purple in Figure 3. Non-prompt leptons, as compared to the prompt leptons resulting from the four dominant channels above, result from either mis-reconstructions or secondary decays of hadrons produced through a different SM interaction. These events will be further detailed and studied in later sections.

1.2.2 Beyond the Standard Model Contributions

The high energy scale of these multi-boson processes, around several hundred GeV and above, also makes four-lepton processes generally more sensitive to models of new physics. BSM contributions can arise from direct leptonic decays of BSM paricles, or through modifications to SM couplings of the Higgs and gauge bosons.

The interference by high energy BSM processes can arise from modifications to the SM couplings. These BSM contributions potentially include cascade decays of new particles introduced by the Minimal Supersummetric SM or additional exotic Higgs doubly-charged scalar bosons [6]. Many BSM models include an additional Z' gauge boson, corresponding to a broken $U(1)$ symmetry, including a scenario in which WIMP-based thermal dark matter couples to the SM via Z' [7]. Such BSM processes would manifest as deviations in high-energy tails of differential cross sections [13]. Four-lepton events therefore present ideal probes of high energy SM physics with precision allowed by charged lepton reconstruction.

2 Apparatus and Data

2.1 The Large Hadron Collider

The search for new physics is done through several types of experiments designed to detect, analyze, and measure particles. Several of these experiments are located at the Large Hadron Collider (LHC) at CERN in Geneva, Swizerland. CERN is Conseil Européen pour la Recherche Nucléaire, or the European Organization for Nuclear Research.

The LHC is a 27 kilometer circular proton-proton collider under the border of France and Switzerland, shown in Figure 4. Beams of protons are accelerated and collided at high energies, reaching center of mass energies around several TeVs, which permits the production of all known SM particles. Such collisions result in a shower of fundamental particles emerging from an interaction point, which leave signals in the detector technology surrounding this point.

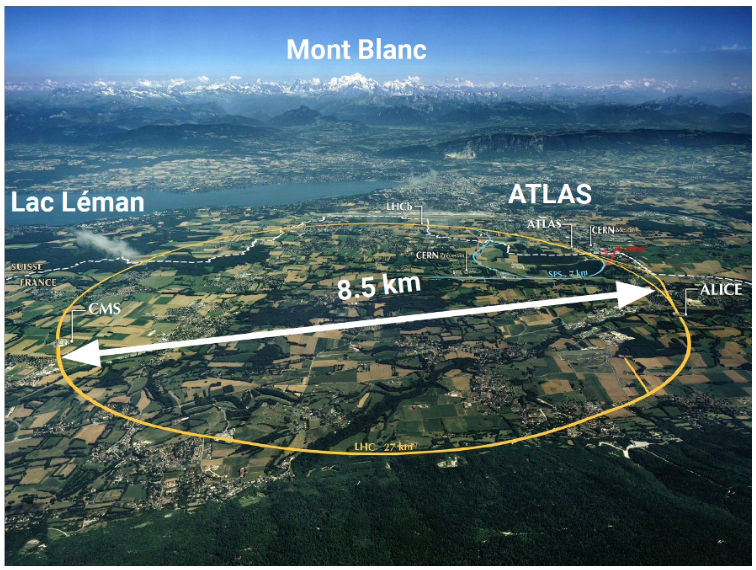

Figure 4: A birds-eye view of the LHC in Geneva, Switzerland. The ring is 27 km in length and 8.5 km in diameter, and is surrounded by several detector experiments, including the ATLAS experiment.

Protons are obtained from hydrogen gas, and accelerated through a series of rings with increasing radii before being sent to the main LHC ring. The high energies effectively decrease the distance scale being probed, that is, allow the observation of particles and interactions on a scale several magnitudes smaller than the radius of a proton [13].

2.1.1 Collider Properties

To specify properties of the LHC, there are a few collider physics quantities that must be defined.

The energy of the collider is defined by $\sqrt{s}$, or the center-of-mass energy, where s is a Mandelstam variable $s = (p_1 + p_2)^2$ for the combined four-momentum p_1 and p_2 of the incoming particles [10]. At the LHC, particles typically have energies ranging from giga-electron volts (GeV) to tera-electron volts (TeV). The data used in this study is from the LHC Run-2, which ran at $\sqrt{s} = 13$ TeV from 2015 to 2018.

Instantaneous luminosity, $\mathscr{L}$, is a measure of the density of the colliding beams. This in part determines the statistical reach of the detector, or the amount of data that may be obtained within a specified amount of time.

More intuitively, luminosity is related to the event count of some interaction, given by

$$N = \sigma \int \mathcal{L} dt,$$

where the integral is with respect to time and σ is the cross section of the particular interaction. Instantaneous luminosity, therefore, has units of $\text{cm}^{-2}\text{s}^{-1}$, so the integrated luminosity is generally measured in inverse femtobarns (fb^{-1}) where 1 fb is 10^{-15} b [10]. For LHC Run-2, 139 fb^{-1} of data was collected.

2.2 The ATLAS Experiment

The ATLAS (**A** **T**oroidal **L**HC **A**pparatu**S**) Experiment is one of several detectors about the LHC, and is built around LHC Interaction Point 1 in Meyrin, Switzerland. A schematic is shown in Figure 5, and the location is shown in Figure 4.

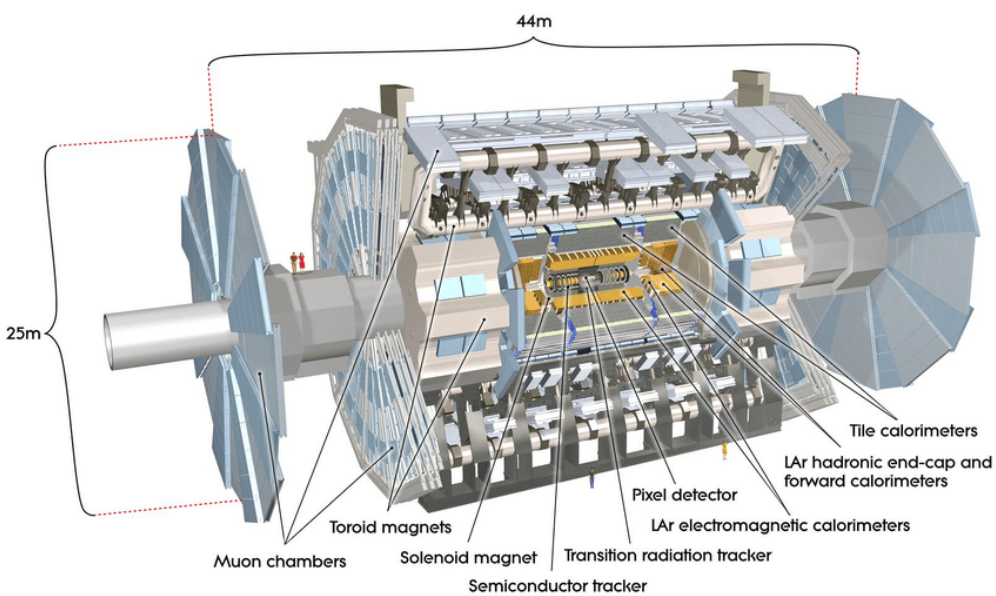

Figure 5: A cross-section schematic of the ATLAS detector and its internal sub-detectors.

The detector consists of concentric cylindrical layers of sub-detectors with forward-backward symmetry, providing a nearly hermetic 4π solid angle coverage around the collision point. It is 44 meters long and has a radius of 12.5 meters. The proton beamline is along the axis of the cylinder. ATLAS is composed of the Inner Detector (ID), electromagnetic (ECAL) and hadronic (HCAL) calorimeters, and an outer Muon Spectrometer (MS).

2.2.1 ATLAS Coordinates

The coordinate system of the detector is right-handed and defined with the longitudinal z axis along the beamline, perpendicular to the transverse xy plane. The x axis is towards the center of the

LHC, and the y towards the surface. The azimuthal angle $\phi \in [0, 2\pi)$ is measured from the positive x axis in the xy plane, and the polar angle $\theta \in [0, \pi)$ is measured from the positive z axis.

Due to the high energy-momentum of the particles, rapidity y is commonly used in collider physics as a measure of the angle between a particle and the beamline, and is defined in terms of the energy and momentum of a particle along the z axis.

$$y = \frac{1}{2} \ln \left(\frac{E + p_z}{E - p_z} \right). \tag{5}$$

Since particles approach the speed of light, $m \ll |\overrightarrow{p}|$ and hence $E \approx |\overrightarrow{p}|$. Rapidity is then approximated by a more easily-measurable value, pseudorapidity η,

$$\eta = \frac{1}{2} \ln \left(\frac{|\overrightarrow{p}| + p_z}{|\overrightarrow{p}| - p_z} \right) = -\ln \left[\tan \left(\frac{\theta}{2} \right) \right]. \tag{6}$$

High values of pseudorapidity indicate forward regions towards the beamline axis, while values close to zero indicate regions near the xy plane [13].

Pseudorapidity is also used to calculate angular separation,

$$\Delta R = \sqrt{(\Delta\eta)^2 + (\Delta\phi)^2}. \tag{7}$$

The momentum of a particle in the transverse direction, p_T, is calculated as

$$p_T = \sqrt{p_x^2 + p_y^2} = p \sin\theta. \tag{8}$$

2.2.2 ATLAS Sub-Detectors

As the innermost sub-detector in ATLAS, the Inner Detector (ID) serves to track charged particles through a magnetic field that are within $|\eta| < 2.5$. The 2 Tesla axial magnetic field is provided by a thin superconducting solenoid. The ID sits 3.3 cm radially away from the beamline and consists of three concentric section that are shown in Figure 6: the Pixel Detector, the Semiconductor Tracker (SCT), and the Transition Radiation Tracker (TRT). As particles pass through the detector layers, a signal will be generated by silicon pixels in the Pixel Detector, silicon-microstrips in the SCT, and straw tubes in the TRT. Since approximately 1000 particles will emerge from the collision point every 25 ns within $|\eta| < 2.5$, fine detector granularity and radiation-hard electronics are required for high-precision measurements. The detector is engineered with tens of millions of micro-strip and micro-pixel silicon sensors, allowing high resolution tracking and micrometer-level uncertainties [3].

The electromagnetic (ECAL) and hadronic (HCAL) calorimeter systems shown in Figure 7 are situated directly outside the ID, and cover the range $|\eta| < 4.9$. The ECAL is divided into a barrel part $|\eta| < 1.475$, and to end-cap parts $1.375 < |\eta| < 3.2$, built from accordion-shaped liquid-argon (LAr) cells and lead absorber plates. In the η region matched to the inner detector, finer granularity provides precision measurements of electrons and photons, while the courser granularity in other regions is sufficient for jet reconstruction. To measure primarily hadronic interactions, the HCAL is composed of a steel scintillating tile calorimeters within $|\eta| < 1.7$, a copper LAr hadronic end-cap calorimeter within $1.5 < |\eta| < 3.2$, and a copper and tungsten LAr forward calorimeter [3].

The outermost Muon Spectrometer (MS) extends to $|\eta| = 2.7$ and measures momenta of muons, which leave only minimum ionizing deposits in the ID and calorimeters. A magnetic field of 0.5 T

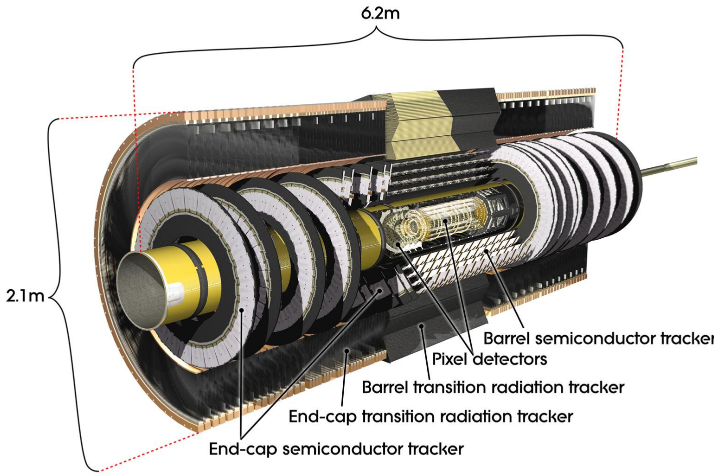

Figure 6: A cross-sectional schematic of the ATLAS Inner Detector, composed of the Pixel Detector, Semiconductor Tracker, and Radiation Tracker.

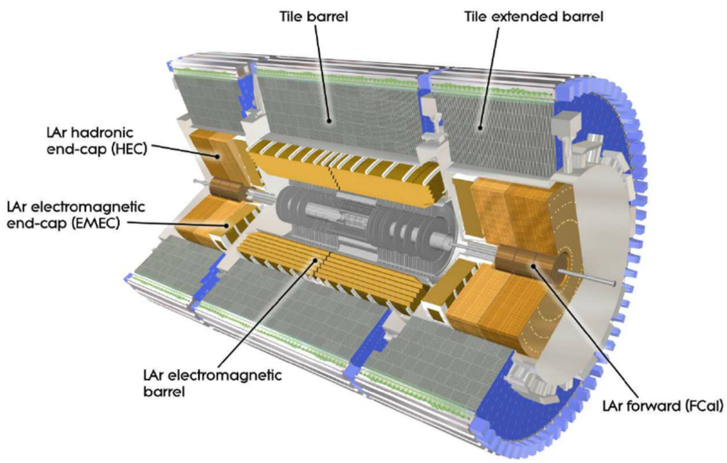

Figure 7: A cross-sectional schematic of the ATLAS electromagnetic (ECAL) and hadronic (HCAL) calorimeter systems.

in the barrel region and 1 T in the end-cap regions is supplied by two end-cap magnets and a barrel toroid magnet. The barrel region extends to $|\eta| = 1.05$, while the remaining are end-cap sections. Monitored Drift Tubes (MDT) and Cathode Strip Chambers (CSC) perform precision tracking, while triggering is done by the Resistive Plate Chambers (RPC) and Thin Gap Chambers (TGC). The schematic is shown in Figure 8.

2.2.3 Trigger and Data Acquisition

The high rate of interactions per bunch crossing is shown in Figure 9, and the 40 MHz frequency of bunch crossing corresponds to 25 ns between successive crossings. This results in up to 1.6 billion collisions per second. With the high level of detail captured by ATLAS, the experiment produces a combined data volume of more than 60 million megabytes per second [2]. This presents an significant challenge, as computational limits do not permit the acquisition of all data produced by the LHC.

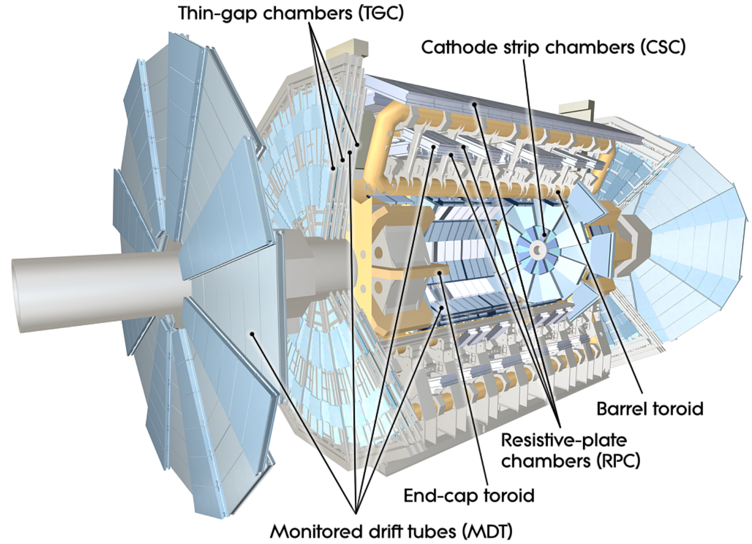

Figure 8: A computer-generated cross-sectional schematic of the ATLAS Muon Spectrometer, showing the four sub-systems.

Instead, the Trigger and Data Acquisition system (TDAQ) ensures optimal data-taking conditions by selectively recording potential processes of interest for later analysis.

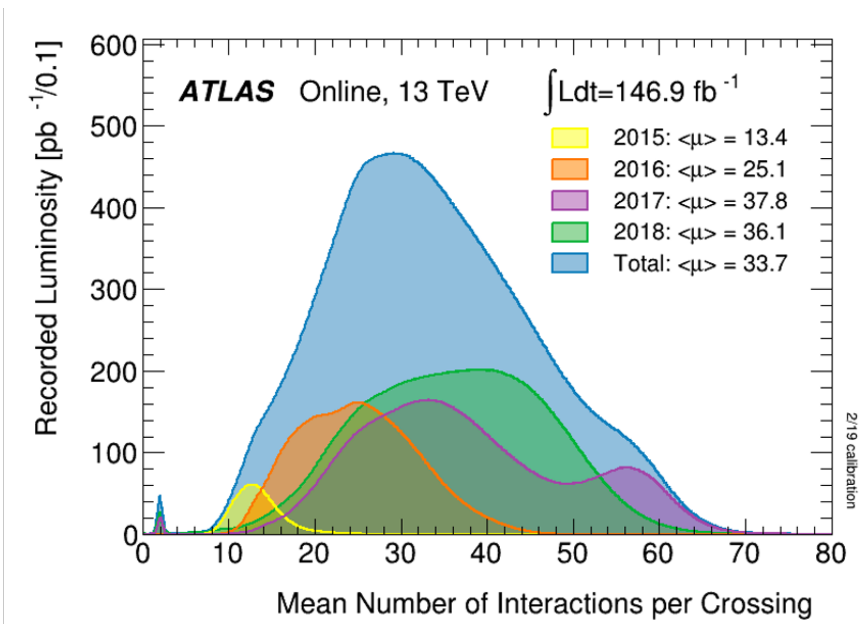

Figure 9: A histogram of integrated luminosity with respect to the mean number of interaction per bunch crossing for years 2015 to 2018. This is a measure of the gradual increase in inelastic simultaneous collisions occurring at the LHC, or pile-up.

The trigger system for Run-2 of the LHC has two distinct levels. The first, L1, is a custom hardware trigger, and uses information from calorimeter and muon systems to provide a coarse event selection by identifying jets, muons, photons, electrons, hadronically decaying τ leptons, and transverse energies [12]. This level reduces the incoming data rate of 40 MHz to 100 kHz [1]. The secondary trigger is a high-level software trigger (HLT) run on high-performance CPU farms with information from L1. This includes a region in the η-ϕ plane, called the Region-of-Interest, where more computationally expensive reconstruction algorithms are run [12]. This reduces the trigger rate to 1.5 kHz [1]. In total, the data is reduced by a factor of about 40,000, allowing these events to be recorded to permanent storage.

2.3 Reconstruction

Understanding how particles interact with the ATLAS detector is key to identifying them and their properties. As particles traverse the detector, they leave behind a series of electrical signals from read-out electronics in the many sub-detectors, creating detector signatures specific to each particle type. Reconstruction is the multistage process by which these raw signatures, in the form of hits and clusters, are translated to well-defined physics objects, such as muons, electrons, photons, and hadronic jets. This done primarily using two techniques: tracking and calorimetry. The first refers to the determination of charged particle trajectories in the ID, whereas the second refers to the analysis of energy deposits in the calorimeters. An example is visualized in Figure 10.

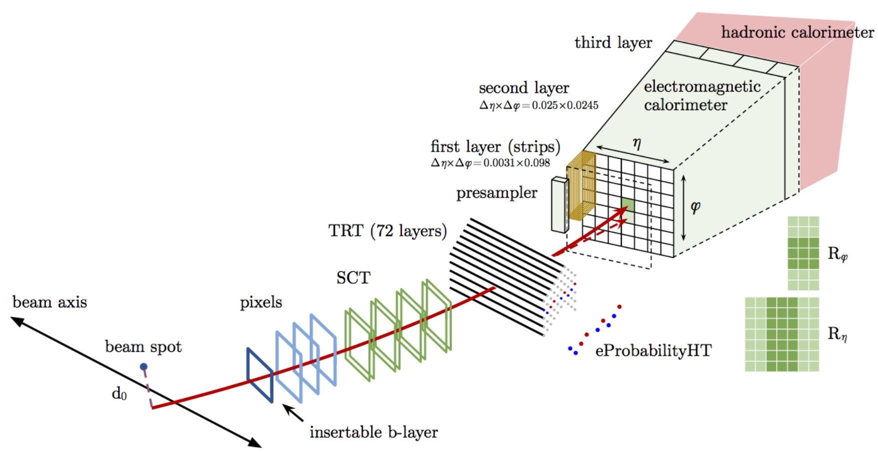

Figure 10: A visualization of how an electron passes through the detector layers and is reconstructed. The particle undergoes tracking using hits generated by the pixels, SCT, TRT. Then, energy deposit showers are measured by the electronic and hadronic calorimeters.

2.3.1 Tracking

In the ATLAS detector, paths of charged particles are curved by a controlled solenoidal magnetic field, and the radius of curvature permits the measurement of particle momentum. Due to the high luminosity there is a significant overlap of simultaneous inelastic collisions, or pile-up. Tracking refers to the process by which raw detector hits in the ID are reconstructed into a collection of tracks left by charged particles. Since traversing detector material influences particle trajectories, the ID is located closest to the beamline to minimize energy loss.

Tracking is crucial in the measurement of particle trajectories and in *vertexing*. Vertexing is the process by which tracks are extrapolated inwards and matched to unique interaction points, or primary vertices. This is key in analysis at the ATLAS detector, particularly due to the multiple vertices resulting from simultaneous pile-up and secondary decay-chain interactions.

Tracks are identified by five parameters and a reference point, using a perigree representation, as visualized in Figure 11. The transverse and longitudinal impact parameters, d_0 and z_0, measure the distance of the single point of closest approach transverse to the reference point. The azimuthal and polar angles are ϕ and θ. Measured through the Lorentz force, the final parameter is proportional to the ratio between the charge of the particle q and its transverse momentum, p_T [5].

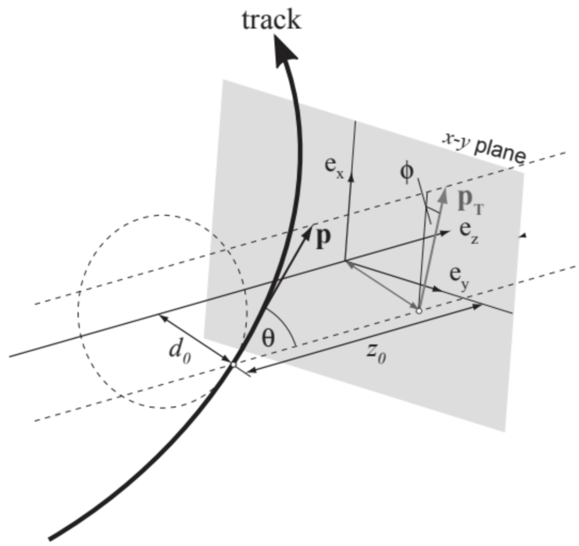

Figure 11: The global track parameters with respect to perigree. The five global helix parameters (d_0, z_0, ϕ, θ, q/p_T) are used to identify the trajectory of a charged particle in a solenoidal magnetic field.

As a brief description of the tracking reconstruction process, Figure 12 summarizes Primary Tracking and Back-Tracking. Primary Tracking is done by constructing space-points from clusters identified by adjacent hits. Triplets of space-points form track seeds, which are extended along potential search roads with a combinatorial Kalman filter. Ambiguities, such as incorrect combinations of unrelated clusters and overlaps between track candidates, are resolved by a neural network based algorithm and a competitive score procedure. Tracks are then re-fit with a global χ^2 method and then extended to the TRT by repeating a similar procedure. Back-tracking is performed, also with a similar procedure, using remaining detector hits to increase acceptance to particles produced at greater distanced from the beamline, e.g. in the detector material [5].

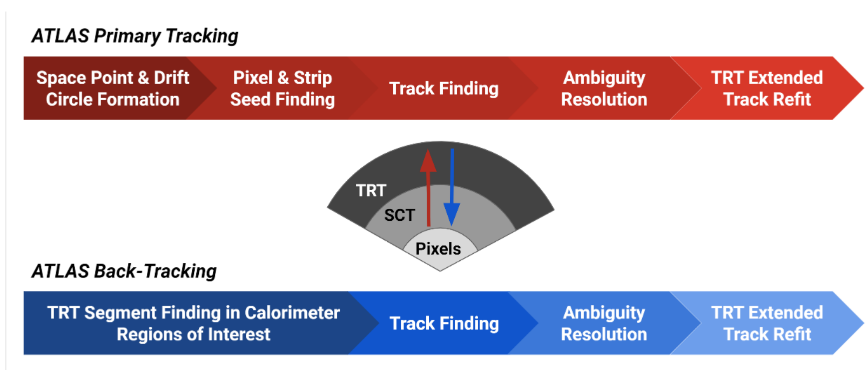

Figure 12: A summary flow chart of the tracking reconstruction process at ATLAS, including Primary Tracking and Back-Tracking.

2.3.2 Calorimetry

The calorimeters have alternating high-density passive material and active material in the $\eta - \phi$ plane, and are segmented into individual cells. Passive layers provide high radiation lengths required to induce electronic and hadronic showers from some incident particle, that is, collimated avalanches of resulting secondary particles, for the active material to detect. The idea is to determine the energy and position of incident particles through measurements of energy deposits via scintillation light or ionization energy [4].

The reconstruction of hadrons and jets is based on three-dimensional topological clustering of individual cell signals. This clustering algorithm identifies topological cell clusters by suppressing noise, or eliminating cells with signals that are not significant and not within close proximity to cells with significant signals. Resulting cluster shape and location provides a well-performing signal definition for jet and missing transverse momentum reconstruction [4].

2.3.3 Particles

Figure 13 illustrates detector signatures of various particle types.

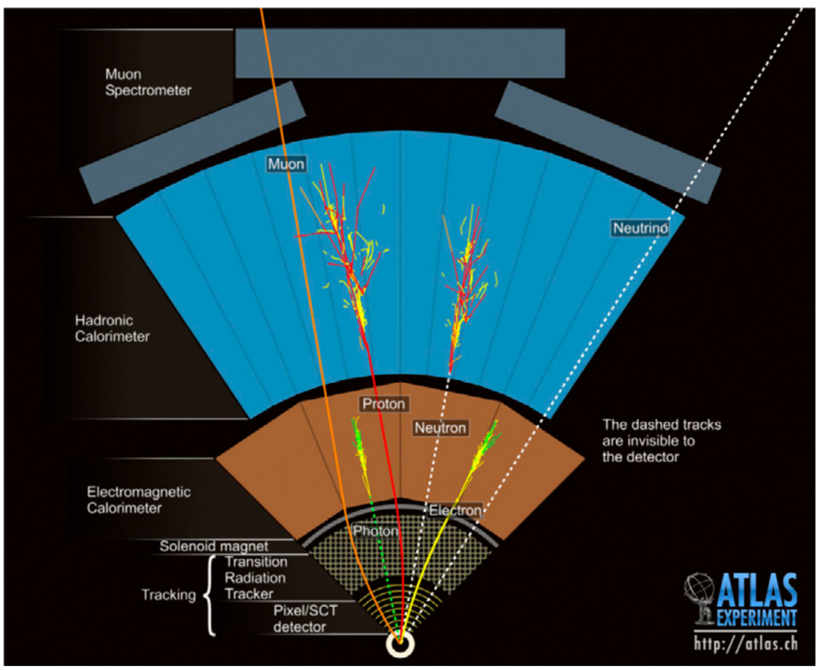

Figure 13: A simplified representation of detector signals left by different particle types in a cross-sectional wedge along the transverse plane of the ATLAS detector.

Charged particles such as protons, muons, and electrons leave tracks in the ID that allow for precise measurements of position and momentum. Photons and electrons induce electromagnetic showers in the ECAL, permitting the measurement of energy. Hadronic jets produced through hadronization of final state partons are absorbed by the HCAL, measuring hadronic activity. The MS provides a secondary and independent measurement of position and momentum of muons to complement the ID. Neutrinos, which are neutral and weakly interaction, do not interact with the detector. To identify neutrinos, missing transverse momentum is measured according to the conservation of momentum in the system.

3 Analysis Strategy

3.1 Four-Lepton Backgrounds

Four-lepton events have final states of two same-flavor, opposite-charge prompt lepton pairs. Due to the rapid decay of the τ lepton, only electrons and muons are considered. Interesting contributions from SM processes, clean background signatures, and sensitivity to BSM processes make four-lepton events ideal candidates for studies of the SM. Data is selected from reconstructed events resulting from Run-2, which ran from 2015 to 2018 at 13 TeV and resulted in 139 fb^{-1} of data.

Prompt leptons in four-lepton events are produced directly from hard-scatter interactions, that is, they result from SM and potential BSM processes of interest. While they allow for a clean separation from otherwise overwhelming backgrounds, *non-prompt* or *fake* leptons produced by secondary hadron decays or as artifacts of mis-reconstructions may still contaminate the four-lepton dataset. Such backgrounds would present as events containing at least one non-prompt lepton, while the remainder of the four leptons are prompt.

These non-prompt leptons are produced mainly in decays of hadrons, produced as by-products in the collisions. They appear with a displacement in relation to the original interaction vertex, since decaying hadrons travel some distance before decaying. Non-prompts are typically surrounded by other charged hadronic particles, due to confinement in QCD. Some examples include pion ($u\bar{d}$, $u\bar{u}$, $d\bar{d}$, or $d\bar{u}$) decay to muon and neutrino, or b quark decay to a muon, neutrino, and c quark.

3.1.1 Background Suppression Strategies

A signal requirement is applied to detect and reject non-prompt leptons. The requirement includes two conditions:

1. **Isolation**: Prompt leptons are required to be isolated from other particles. Their isolation is tested with a scalar sum of the transverse momenta of all charged particles within a cone of $\Delta R = 0.3$ around the lepton. If the ratio between this sum and the transverse momentum of a lepton is greater than 0.16, then this lepton is rejected [6].

2. **Track-to-Vertex Association (TTVA)**: TTVA refers to the closest approach of the lepton track to the primary vertex, measured through impact parameters d_0 and z_0. Prompt leptons originate from massive gauge bosons, which have a short lifetime on the order of 10^{-25} seconds. Thus, once they decay, these bosons would have traveled short enough distance such that their decay products appear to have originated from the original proton-proton interaction within the resolution of the detector. Impact parameters are therefore expected to be very small for prompt leptons, and leptons with non-zero d_0 or z_0 are suppressed.

Leptons that are isolated and have vanishing impact parameters are classified as *signal* leptons and are expected to be mostly prompt, whereas leptons that do not satisfy at least one of the requirements are classified as backgrounds. Figure 14 demonstrates an example of a muon that fails both suppression requirements.

The idea of applying the signal requirements is to allow nearly all prompt leptons to pass while rejecting non-prompts. However, while effective, these cuts are not 100 percent efficient at removing backgrounds and some non-prompt leptons will remain in the dataset.

A precise understanding of these residual non-prompt backgrounds is becoming more essential with the increasing statistical precision on the measurements allowed by the growing LHC dataset. The

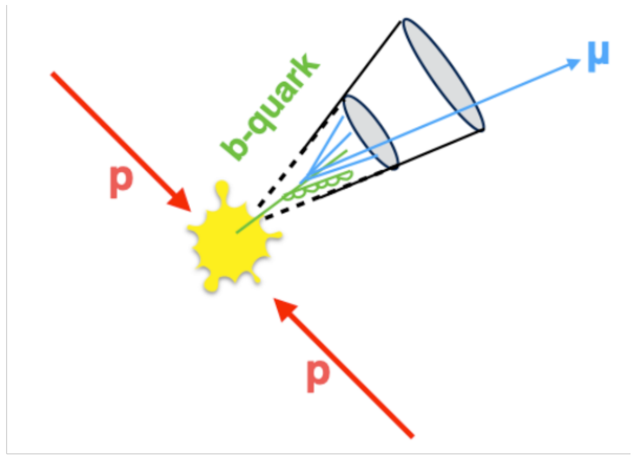

Figure 14: A simple depiction of a muon, in blue, that fails both isolation and TTVA from the signal requirements. There is high activity in the cone surrounding the muon, and the track does not trace back to the original proton-proton interaction point.

ultimate goal is therefore to apply signal requirements, estimate the ratio of remaining non-prompts, and subtract them from the dataset. Remaining data will represent the distribution of prompt four-lepton events occurring at the LHC.

3.2 Data-Driven Fake Factor Analysis

While increasingly accurate theoretical calculations are available to model rare processes which produce genuine four-lepton events, properties of other non-prompt lepton backgrounds are difficult to predict from theory alone. This is because such events include rare detector effects, such as mis-reconstructions, which are challenging to simulate with high accuracy. Thus, these backgrounds are preferentially evaluated from collision data. This method is called data-driven Fake Factor analysis.

The fake factor (F) is defined as the ratio of non-prompt leptons passing the signal requirement to the non-prompt leptons rejected by the signal requirement. The fake efficiency (f) denotes the probability that a non-prompt lepton is incorrectly labeled as signal. Fake factor is related to fake efficiency by

$$F = \frac{f}{1-f}. \tag{9}$$

A major goal of Fake Factor analysis is to estimate fake efficiency, so that non-prompt backgrounds passing the signal requirement may be subtracted from the four-lepton dataset. To decrease the effects of background contamination and enable more precise analysis in the search for new physics at the LHC, properties of non-prompt leptons are studied and uncertainties on the fake efficiency reduced.

3.2.1 Fake Efficiency Estimates

Fake efficiency is defined as the probability that a lepton passes the signal requirement, given that it is non-prompt. In other words, it measures the ratio of non-prompt leptons that get past signal requirements. This can be simply measured as the number of leptons that are non-prompt and pass the signal requirement, divided by the number of non-prompt leptons.

More precisely, the fake efficiency is measured as:

$$
\begin{aligned}
f_{\text{data}} &= \frac{\text{number of non-prompt leptons classified as signal}}{\text{number of non-prompt leptons}} \\
&= \frac{\text{baseline signal leptons} - \text{classified prompt signal leptons from MC}}{\text{all baseline leptons} - \text{classified prompt leptons from MC}},
\end{aligned}
\tag{10}
$$

where baseline leptons form a pre-selected sample from the reconstruction of a particular process. Since the particular physics process contributing to a specific collision event is not known, Monte Carlo (MC) simulations of particle-detector interactions are used to estimate and subtract prompt lepton contributions. Then, the remaining leptons are expected to be non-prompt, yielding an estimate for the number of non-prompt leptons. This is done for non-prompt leptons passing the signal requirement in the numerator, and for all non-prompt leptons in the denominator.

In four-lepton events, the fake efficiency is used to estimate the ratio of reconstructed signal events containing one or more non-prompt leptons. Then, after subtracting these non-prompt backgrounds, the distribution of prompt leptons can be more accurately determined. To estimate fake efficiency, samples of dilepton events are used. In particular, I analyze decays of the Z boson or two top quark pairs to two opposite-charge leptons. This sample has the important property that any third additional leptons in reconstructed events from the dilepton sample are likely to appear as non-prompt. These additional leptons therefore form an ideal baseline lepton sample with a relatively high ratio of non-prompt leptons for the study of non-prompt lepton behaviors.

3.2.2 Fake Efficiency Uncertainties

In the calculation of fake efficiency, the MC contribution estimates and subtracts any prompt leptons in the sample that would otherwise falsify the measurement. However, the MC also contributes to systematic uncertainty in the measurement of fake efficiency, forming the primary source of uncertainty as shown in Figure 15. Uncertainties in the MC are due to the limited precision of underlying theoretical calculations. Sources of systematic uncertainties include calculations of the parton distribution functions (PDF), QCD scale, and the strong coupling constant α_s. Properties of non-prompt leptons are therefore be studied to reduce systematic uncertainties resulting from MC estimation of prompt leptons. By applying selections to the sample, I reduce the number of events with prompt additional leptons, thereby reducing the MC contribution in the fake efficiency estimate.

3.3 Monte Carlo Simulation

Events are predicted using Monte Carlo (MC) simulations, generated primarily with Sherpa 2.2.0-2.2.2. Simulation used to obtain SM predictions for various measurements. It starts by simulating the physics of the particle interactions, which gives a list of particles with associated momenta and directions. These are plugged into a detector simulation, which emulates how ATLAS will respond to the particles. The predicted detector response can be plugged into the standard event reconstruction, just as it is done for real collision data. The output is the predicted outcome of our measurements, based on the a given model. The difference is that in simulated data, the original process that caused the signal is known.

However, simulation is not necessarily guaranteed to be representative of the data. The final measurement of fake efficiency therefore has to be done with data, hence the data-driven analysis.

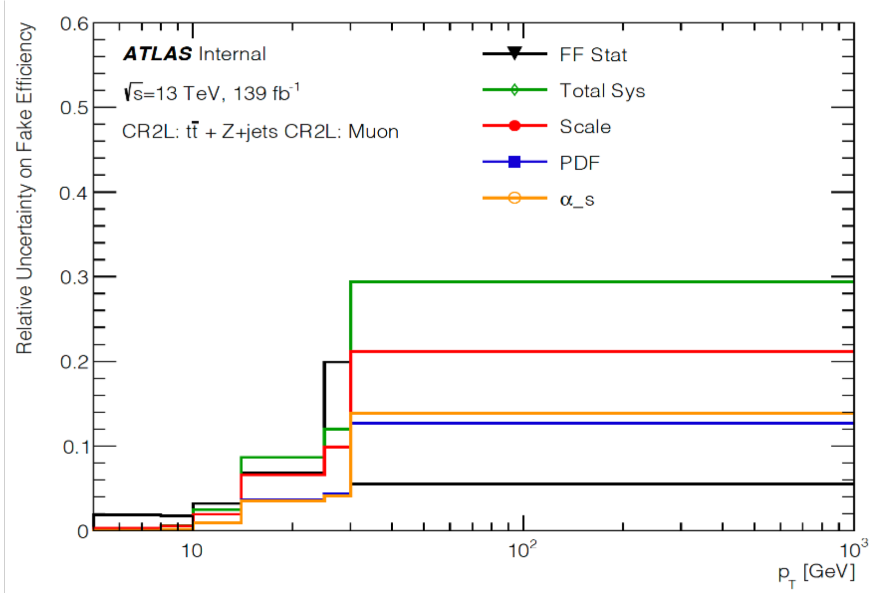

Figure 15: A plot of various relative uncertainties in the fake efficiency calculation with respect to transverse momentum. The total systematic uncertainty is shown in green, and statistical uncertainties are in black.

The advantage of MC simulation is that it allows tests that are not possible in data. Reconstructed particles can be matched to the simulated particles, thus providing some indication of what is prompt and non-prompt. A "true" value of fake efficiency can be found from the simulation by checking how many generated non-prompt leptons are classified as signal and then comparing this to our measurement.

3.4 Preliminary Sample Selection

Histograms of events are plotted with respect to various kinematics and other observables to study and visualize lepton samples. Observables include particle type, particle momenta, isolation, impact parameters, trajectory angles, and reconstructed invariant masses. To make selections, thresholds on particle kinematics or other observables that individual particles must meet are applied to datasets. Particles outside of the thresholds are rejected. Such requirements are called selection *cuts*.

In order to study the properties of non-prompt leptons, samples of reconstructed dilepton events having additional third or fourth leptons have been extracted. These events provide a well-understood sample of collision data in which the appearance of an additional, third lepton is most likely in the form of a non-prompt lepton. The two primary processes contributing to this region, Z boson decay and top quark pair decay ($t\bar{t}$), are separated and analyzed individually.

The **Z boson** may decay to two leptons by three modes: $Z \to e^-e^+$, $Z \to \mu^-\mu^+$, and $Z \to \tau^-\tau^+$. The first two simply decay by a single vertex, as in Figure 16. Tau leptons are not stable, so they decay further into neutrinos and an electron or muon pair. The Z boson itself is typically produced by a quark-antiquark pair.

The $t\bar{t}$ **events** result from the decay of a gluon, which generally result from the interaction of two other gluons or quark-antiquark pair. The Feynman diagram is shown in Figure 17, where the decay results in an electron or muon pair in addition to a couple of b quarks and neutrinos.

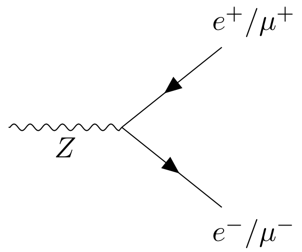

(a) $Z \to e^-e^+$, $Z \to \mu^-\mu^+$

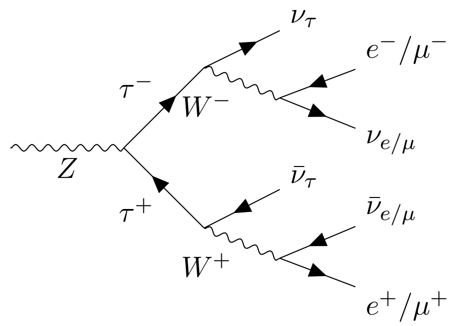

(b) $Z \to \tau^-\tau^+$

Figure 16: Feynman Diagrams of Z boson decays. Three decay modes are shown: $Z \to e^-e^+$, $Z \to \mu^-\mu^+$, and $Z \to \tau^-\tau^+$. The first two are relatively stable as the electrons and muons traverse the detector, but the τ leptons decay to their more stable counterparts.

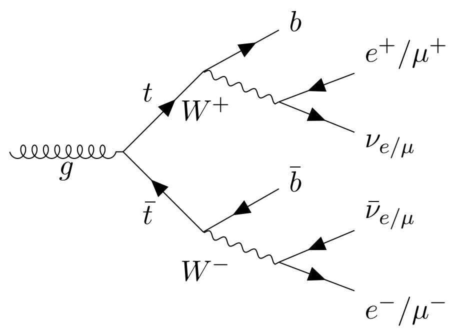

Figure 17: A Feynman Diagram of a $t\bar{t}$ decay. A gluon decays to a top and anti-top quark, which each decay into a b quark and a more stable lepton-neutrino pair via a W boson.

I perform the separation between the two regions primarily through lepton flavor, where Z boson events decay to same-flavor pairs (ee and $\mu\mu$) and $t\bar{t}$ events produce both same- (ee, $\mu\mu$) and different-flavor pairs ($e\mu$) equally. The $t\bar{t}$ region in this case is identified by decays to $e\mu$.

In addition to the cut on lepton flavor in the Z boson region, I select events having invariant mass $m_{\ell\ell}$ in the region closest to the Z boson invariant mass m_Z (between 60 and 120 GeV). This effectively removes remaining $t\bar{t}$ events using the same-flavor opposite-charge mass window. Comparing the two regions serves the role of probing different collision environments.

While additional leptons are expected to be non-prompt, a small portion of additional leptons were prompt. These arise from mis-reconstructions, detector effects, WZ decay, or other processes. To perform an accurate analysis of the fake efficiency in these regions, my initial goal is to suppress prompt sources. Comparisons to Monte Carlo (MC) simulated data from Z boson, $t\bar{t}$, and WZ events provide correction factors and estimations on data composition.

4 Results and Interpretation

Data in this section is visualized with histograms and ratio plots. The histograms show event distribution across some kinematic observable, with the real collision data shown in black and MC simulations as stacked colored histograms. Ratio plots show the ratio of data with respected to the total MC events.

4.1 Sample Purification

My goal is to suppress prompt sources and obtain a sample as pure as possible in non-prompt leptons. This sample may be used to estimate the fake efficiency. By doing this, the systematic uncertainty resulting from the prompt lepton estimate of the MC in the fake efficiency estimate is reduced, and the behaviors of non-prompt leptons is studied.

4.1.1 Z Boson Sample

From a preliminary analysis, the primary source of prompt additional leptons in Z boson events is from WZ events. These events decay with a very brief lifetime, and result in a third additional prompt lepton coming from the interaction vertex. Figure 18 shows the transverse momentum distribution of additional leptons passing the signal requirement for the selected Z boson decays, as well as the MC prediction from specific processes.

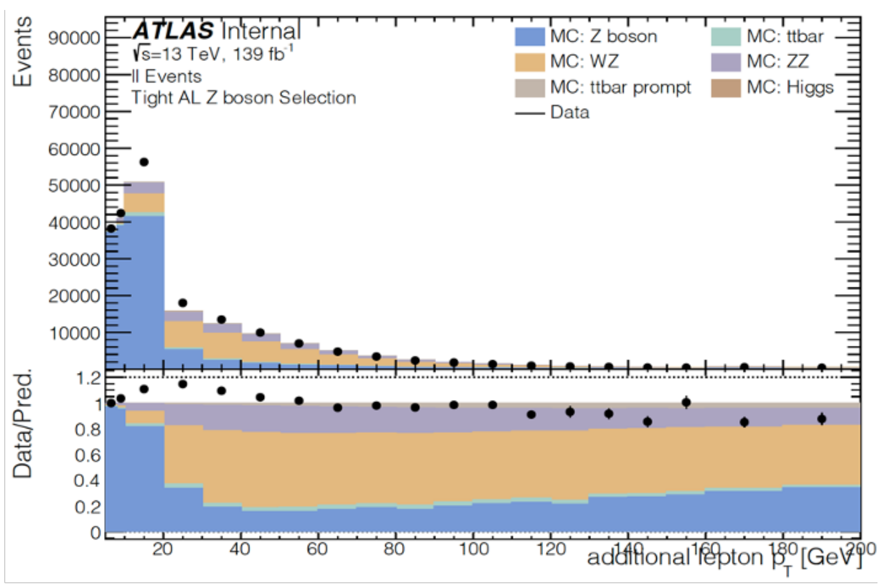

Figure 18: Transverse momenta of additional leptons passing signal requirement in the Z boson sample. Black dots represent collision data. Stacked colored histograms represent MC prediction of Z boson events, $t\bar{t}$ events, and WZ events.

To suppress WZ events, I investigate a variety of cuts on kinematic variables. A particularly efficient cut is determined from Figure 19. The transverse mass of additional leptons in WZ events peak around 80 GeV, close to the W mass, while Z boson events peak closer to zero. Since WZ event make up the majority of the data for $m_T > 50$ GeV, I applied a cut to remove these events from the data.

I use similar logic for other kinematic variables, such as dilepton invariant masses, transverse

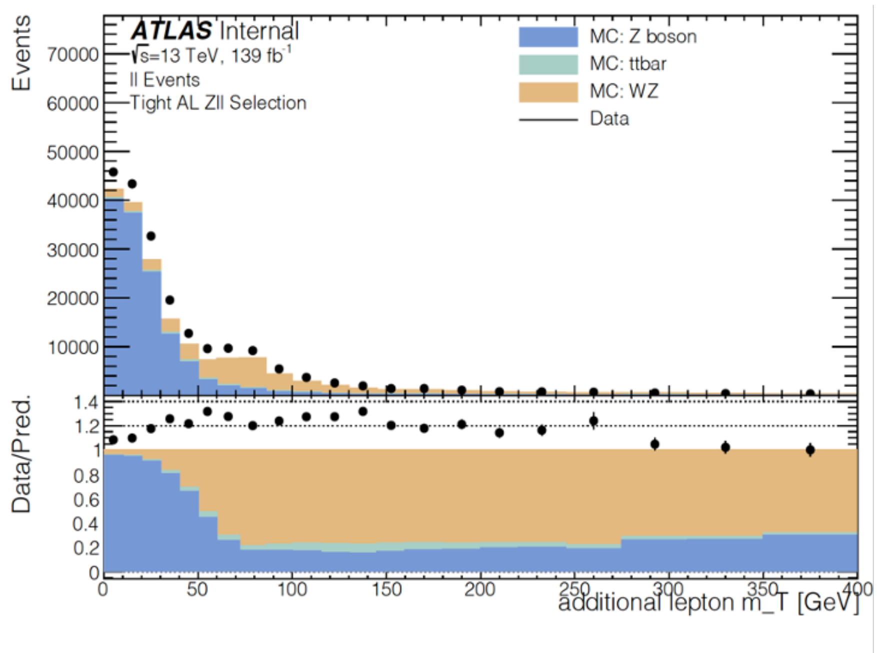

Figure 19: Transverse mass of additional leptons in the Z boson sample. The majority of data above 50 GeV results from WZ events, based on MC prediction.

momenta, and angular correlation variables. The effectiveness of these other cuts are significantly less than the cut on transverse mass.

Variable	Cut
additional lepton m_T	< 50 GeV
dilepton angular separation (dR)	> 0.8
pair lepton p_T	< 200 GeV
2nd lepton p_T	< 70 GeV

Table 2: Suppression cuts for Z boson.

Table 2 shows the suppression cuts applied to the dataset. After application of the suppression cuts from table 2, Figure 20 shows that the region is purer in Z boson events as predicted by the MC. This implies that the sample consists of a higher fraction of non-prompt leptons.

4.1.2 Top Quark Sample

The preliminary study of this $t\bar{t}$ sample, containing opposite-flavor dilepton events with additional leptons, shows evidence of prompt leptons from both WZ events. In addition, I identified an unexpected source of mis-reconstructions. This presents itself as a large fraction of Z boson events in the $t\bar{t}$ (i.e. opposite-flavor, $e\mu$) region.

After breakdown of Z boson decays to individual processes ($Z \to \tau\tau$, $Z \to \mu\mu$, and $Z \to ee$), Figure 21 shows evidence of unexpected, substantial contamination of $Z \to \mu\mu$ events in the $e\mu$ decay region. The associated additional leptons in these events appear to be a muon. This suggests that of the two muons, one is being paired with some electron while the other is flagged as an additional lepton.

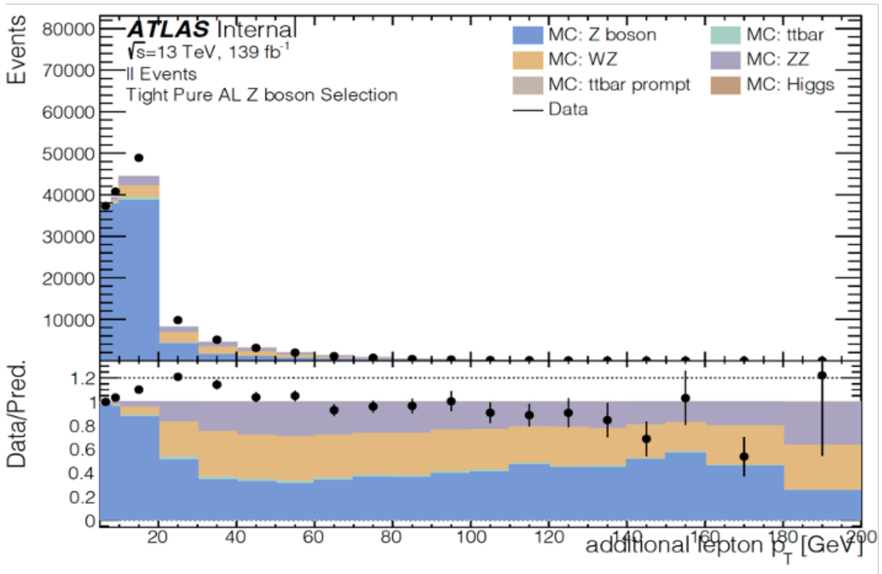

Figure 20: Transverse momenta of additional leptons in the Z boson sample after the application of selection cuts listed in table 2.

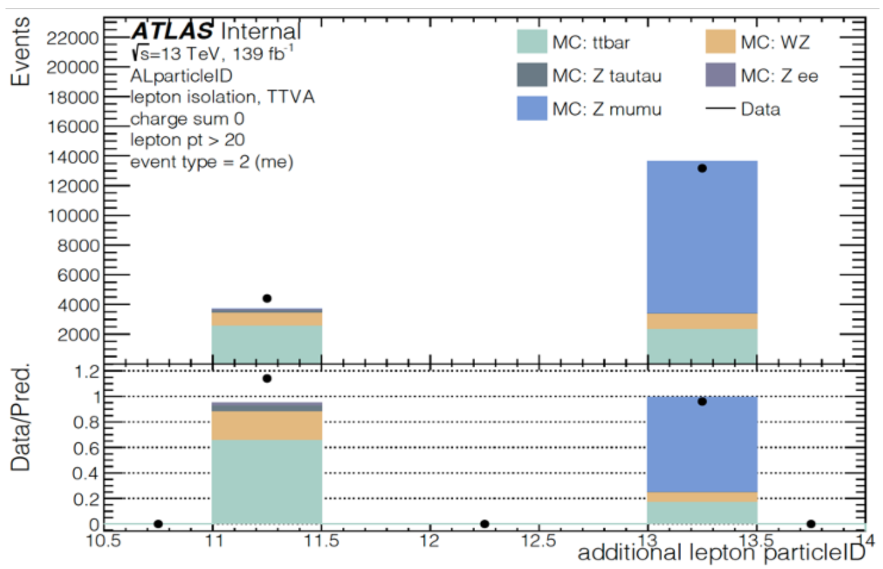

Figure 21: Particle type of the additional leptons in the $t\bar{t}$ region. The bin at 11 corresponds to the number of additional leptons that are electrons, and the bin a 13 corresponds to the number of additional leptons that are muons.

Furthermore, the m_{SFOS}, i.e. the mass of same-flavor opposite-sign pairs closest to that of the Z boson, is shown in Figure 22 and implies that the paired electron is in reality a photon mis-reconstructed as an electron. It is expected that Z boson events would peak about 90 GeV; the lower peak implies that mass was carried away by a third particle, the photon that was reconstructed as an electron. The expected mass of 90 GeV describes that of $\mu\mu$ and the photon. The data that does exist about 90 GeV is likely from events in which a non-prompt electron passes the signal requirement.

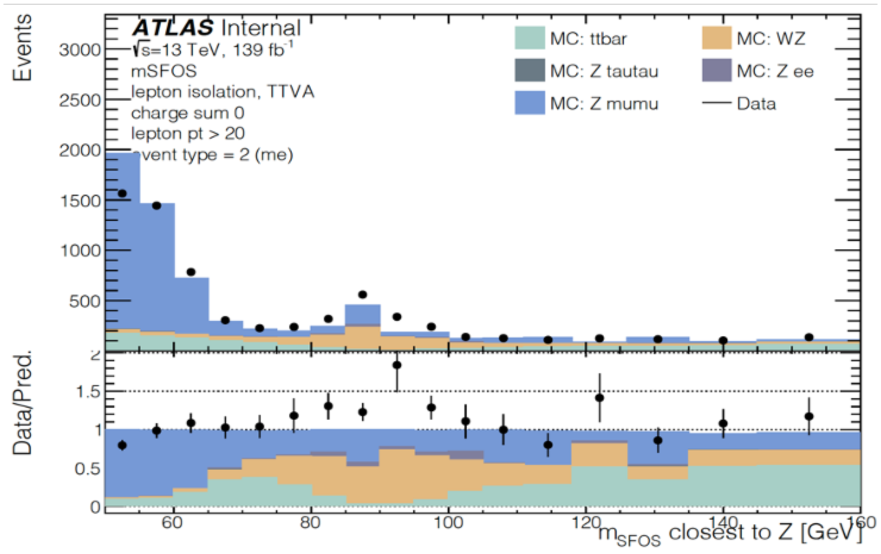

Figure 22: The m_{SFOS} closest to Z, or the mass of same-flavor opposite-sign pairs closest to that of the Z boson, in the $t\bar{t}$ region. Z boson events are generally expected to peak around the Z boson invariant mass of about 90 GeV, but instead a significant contribution of Z boson events are observed at lower masses.

To suppress this, I applied an existing SignalID requirement to both leptons in the pair. SignalID is designed to reject photons mis-reconstructed as electrons through signatures reconstructed in the electromagnetic calorimeter, and its application significantly reduces the Z boson contribution in the $t\bar{t}$ region. This validates the previous mis-reconstruction theory.

The suppression of remaining prompt sources from Z and WZ boson events is performed as they were for the Z boson region. Figure 23 shows the distribution of transverse momenta of additional leptons passing the signal requirement for the selected $t\bar{t}$ decays.

To suppress Z boson and WZ events, I investigate a variety of cuts on kinematic variables. A particularly efficient cut is shown in figure 24. The $t\bar{t}$ event is expected to produce two b quarks, so eliminating events without b-tagged jets proved highly effective.

I use similar logic for other kinematic variables, such as dilepton invariant masses, transverse momenta, and angular correlation variables.

Variable	Cut
b-tag	> 0
m_{SFOS} closest to Z	> 80 and < 100 GeV

Table 3: Suppression cuts for $t\bar{t}$ events.

Table 3 shows the suppression cuts applied to the dataset. After application of the suppression cuts from table 3, Figure 25 shows the sample to have a significantly greater ratio of $t\bar{t}$ events and thus a high fraction of non-prompt leptons as predicted by the MC.

4.1.3 Re-Iteration

In both Z boson and $t\bar{t}$ samples, the discrepancy between data and MC predictions in both regions suggests that the MC does not perfectly describe non-prompts. A few additional processes (such as

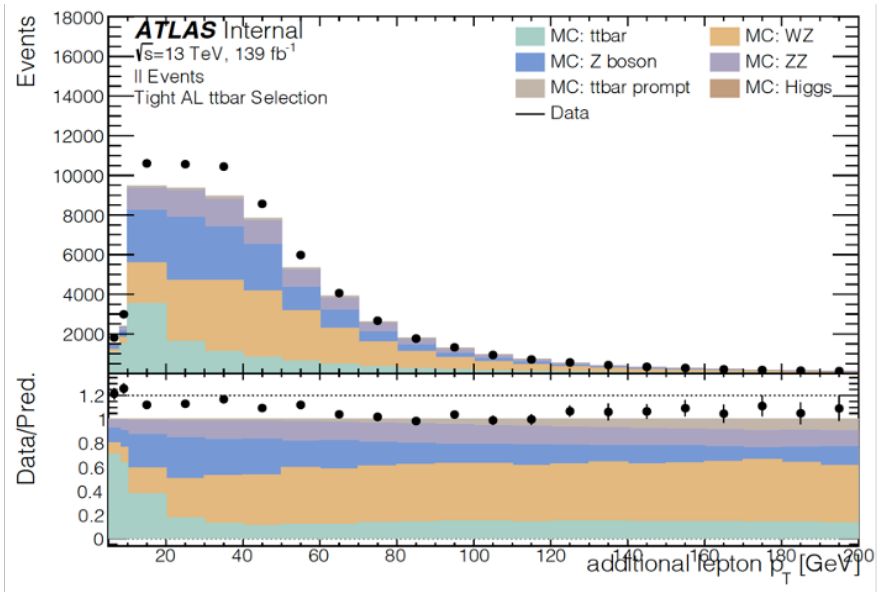

Figure 23: Transverse momenta of additional leptons passing signal requirement in the $t\bar{t}$ sample. Black dots represent collision data. Stacked colored histograms represent MC prediction of Z boson events, $t\bar{t}$ events, and WZ events.

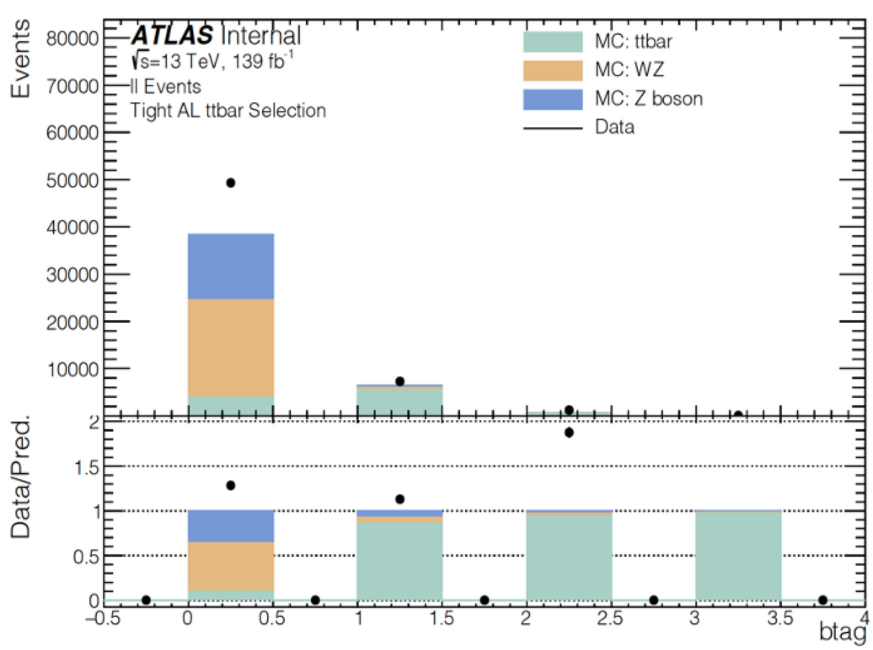

Figure 24: The b-tagging in the $t\bar{t}$ sample. Nearly all prompt and Z boson event contaminants have no b-tags.

the Higgs decay) were added to the MC.

Suppression of prompt sources demands a balance between systematic and statistical uncertainty. Strict cuts to eliminate prompt sources reduce systematic uncertainty, as it reduces the MC terms the fake efficiency estimate. However, this also reduces sample size, which increases statistical uncertainty. I re-iterated this study on sample purification to produce the above presented results,

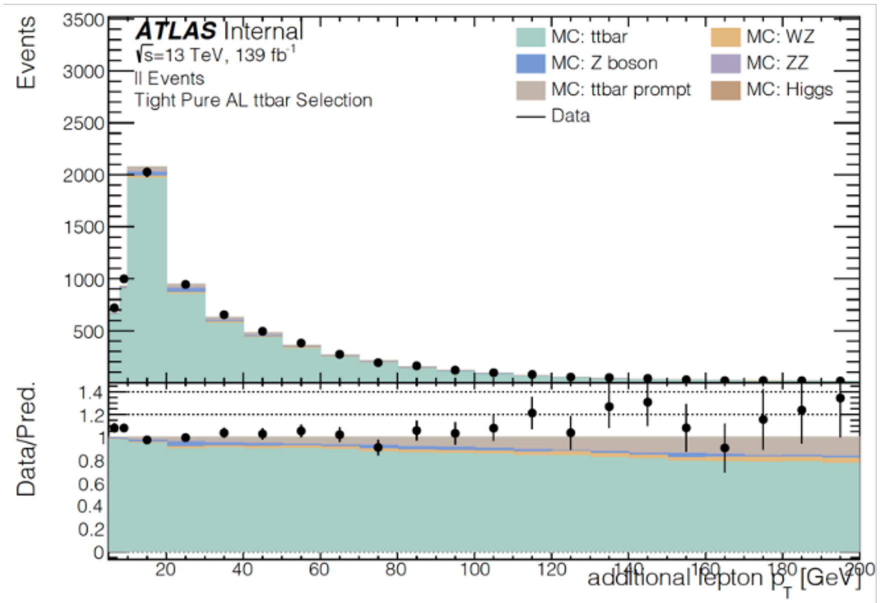

Figure 25: Transverse momenta of additional leptons in the $t\bar{t}$ sample.

experimenting with cuts on various kinematic observables to minimize systematic uncertainty without sacrificing statistical precision.

4.2 Rejection Power

To examine rejection power for frequently used analysis cuts, I estimate and plot fake efficiency for both both regions across kinematic variables.

In some cases, there is a real dependence of fake efficiency on kinematics. For example, in Figure 26, fake efficiency worsens with greater p_T because leptons with greater transverse momentum are more likely to pass signal requirements.

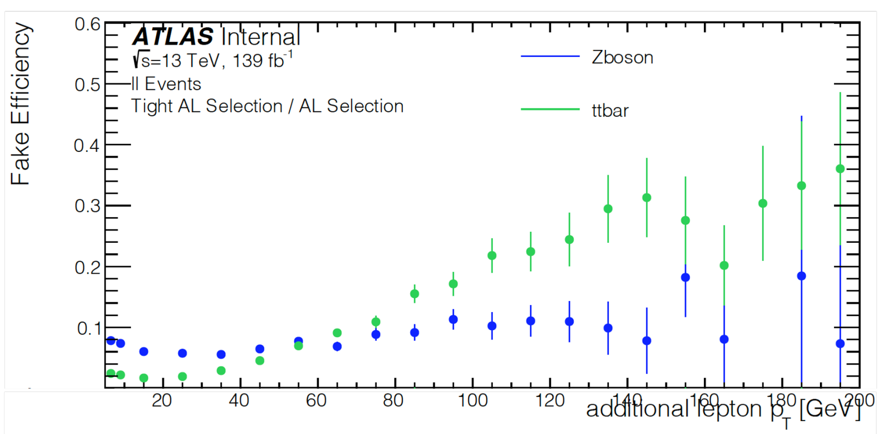

Figure 26: Estimation of Fake Efficiency over p_T.

Since Z boson and $t\bar{t}$ samples probe different compositions of non-prompt leptons, it is expected that they would yield different results. Any differences between Z boson and $t\bar{t}$ regions is a measure of how strongly fake efficiency depends on the sample composition.

4.3 Reduced Uncertainties

My studies show that the most effective cut to suppress prompt leptons in the Z boson, or Z + jets, control region is $m_T < 50$ GeV. For the $t\bar{t}$ region, it is the requirement that the number of b-tagged jets is at least one.

Figures 27 and 28 show the effect of applying these cuts on the Z + jets and $t\bar{t}$ control regions [9]. The systematic uncertainties on the calculation of fake efficiency in each region have been greatly reduced up to and around a factor of ten.

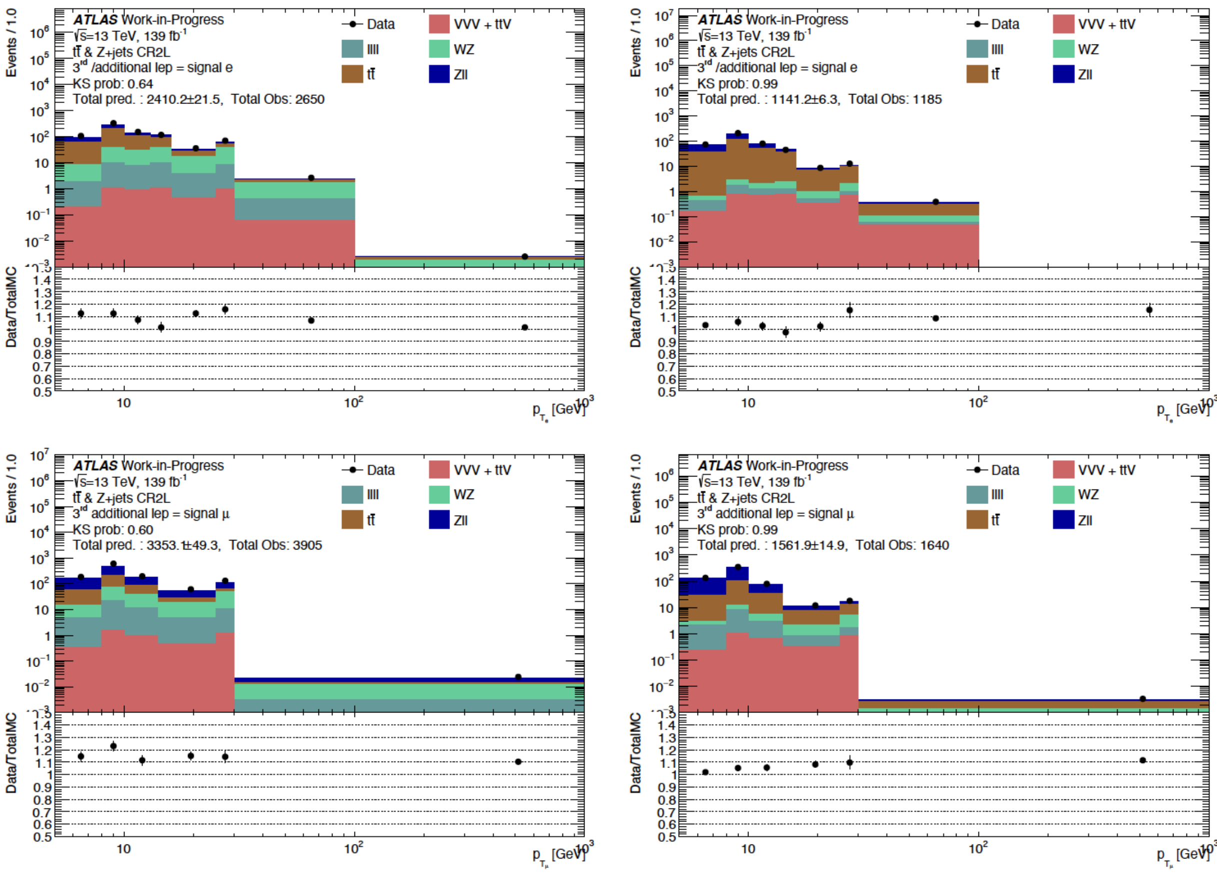

Figure 27: Yield of the additional electrons (top) and muons (bottom) passing the signal requirement in the combined region before and after applying $m_T < 50$ GeV to the Z + jets control region and a b-jet tagging requirement to the $t\bar{t}$ control region. The yield of additional leptons passing the signal requirement is shown before (on the left) and after (on the right) application of cuts.

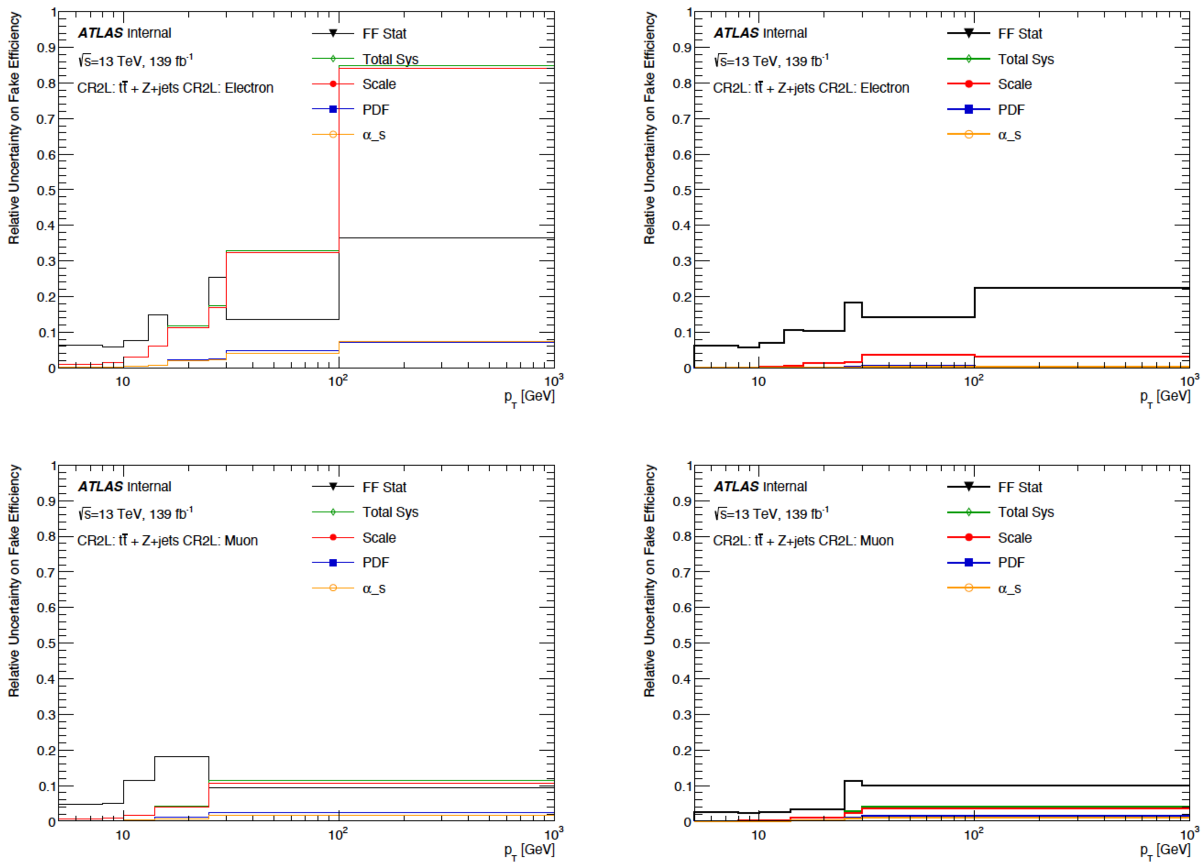

Figure 28: Systematic uncertainties of the additional electrons (top) and muons (bottom) passing the signal requirement in the combined region before and after applying $m_T < 50$ GeV to the Z + *jets* control region and a b-jet tagging requirement to the $t\bar{t}$ control region. The uncertainties of additional leptons passing the signal requirement is shown before (on the left) and after (on the right) application of cuts.

5 Conclusions

The four-lepton final state, characterized by the clean signature of two same-flavor, opposite-charge lepton pairs, offers an excellent avenue for precision tests of the Standard Model at the ATLAS experiment about the Large Hadron Collider. Several interesting Standard Model and Beyond the Standard Model processes originating from hard-scatter proton-proton interactions contribute to these events. However, the dataset may still be contaminated by non-prompt leptons, which originate from secondary hadron decays and mis-reconstructions. Through analysis of two dilepton samples from real collision data and Monte Carlo simulated predictions, specifically the Z boson and $t\bar{t}$ decay to two opposite-charge leptons, the behavior of non-prompt leptons and their respective suppression strategies were studied.

The fake efficiency is the fraction of non-prompt backgrounds remaining after the application of the suppression signal requirements. By applying a transverse momentum and ($m_T < 50$ GeV) and a b-tagged jets (b-tag > 0) cut in the Z boson and $t\bar{t}$ control regions respectively, the relative systematic uncertainty, which results from theoretical uncertainties in the Monte Carlo contribution, on the fake efficiency estimate is reduced by roughly a factor of ten. As a result of this study, the purity of these Z boson and $t\bar{t}$ control regions have been significantly improved, which will prove useful in extensions of background estimates and four-lepton analysis at ATLAS. This increased precision will allow further searches for new physics Beyond the Standard Model.

Acknowledgements

A huge thank you to Dr. Gabriella Sciolla for the research opportunities and incredible mentorship, Dr. Max Goblirsch for his guidance every step of the way, and finally Prajita Bhattarai for setting up the files, helping to estimate uncertainties, and answering myriad of questions. I would also like to thank Dr. Gabriella Sciolla and Dr. Aram Apyan for serving on my thesis committee.

Thank you to the US ATLAS SUPER program as well as Brandeis University for the funding, mentorship, and presentation opportunities throughout my undergraduate career.

Most of all, thank you to the family, friends, and mentors who had faith and invested in me. I couldn't have done it without all of you.

References

[1] ATLAS Collaboration. Approved plots daq (run-2). https://twiki.cern.ch/twiki/bin/view/AtlasPublic/ApprovedPlotsDAA.

[2] ATLAS Collaboration. Trigger and data acquisition. https://atlas.cern/Discover/Detector/Trigger-DAQ.

[3] ATLAS Collaboration. The atlas experiment at the cern large hadron collider. *JINST*, August 2008.

[4] ATLAS Collaboration. Topological cell clustering in the atlas calorimeters and its performance in lhc run 1. *Eur. Phys. J. C 77 (2017) 490*, (10.1140/epjc/s10052-017-5004-5), August 2017. arXiv:1603.02934.

[5] ATLAS Collaboration. Atlas track reconstruction, 2021. ATLAS Software Documentation: https://atlassoftwaredocs.web.cern.ch/trackingTutorial/idoverview/.

[6] ATLAS Collaboration. Measurements of differential cross-sections in four-lepton events in 13 tev proton-proton collisions with the atlas detector. JHEP 07 (2021) 005(10.1007/JHEP07(2021)005), July 2021. arXiv:2103.01918.

[7] J. A. Aguilar-Saavedra et al. Multilepton dark matter signals. *Journal of High Energy Physics*, April 2022.

[8] P.A. Zyla et al. (particle data group). Prog. Theor. Exp. Phys., 2020. 083C01 (2020) and 2021 update.

[9] Z. Schillaci et al. Measurements of differential cross-sections for the inclusive and the electroweak production of zz in association with two jets in four-lepton events in 13 tev proton-proton collisions with the atlas detector. ANA-STDM-2020-02-INT1, March 2022.

[10] David Griffiths. *Introduction to Elementary Particles*. Wiley-VCH, Weinheim, Germany, 2nd edition, 2008.

[11] David J. Griffiths and Darrell R. Schroeter. *Introduction to Quantum Mechanics*. Cambridge University Press, New York, NY, 3rd edition, 2018.

[12] Catrin Bernius (SLAC) on behalf of the ATLAS Collaboration. The atlas trigger & data acquisition (tdaq) system, 2020. Slides from Mu2e-II Workshop.

[13] Zach Michael Schillaci. *Precision measurements of four-lepton production in $\sqrt{s} = 13$ TeV proton-proton collisions with the ATLAS detector*. PhD thesis, Brandeis University, Waltham, MA, August 2021.